


## Bias-Polarity-Dependent Photocurrent Spectra of Terahertz Stepped-Quantum-Well Photodetectors

GuiXue Zhang,<sup>1</sup> XuGuang Guo<sup>1,\*</sup>, HaiXia Wang,<sup>2</sup> DiXiang Shao,<sup>1,2</sup> ZhangLong Fu,<sup>2,3</sup> ZhiYong Tan,<sup>2,3</sup> Hua Li,<sup>2,3</sup> JunCheng Cao,<sup>2,3</sup> and YiMing Zhu<sup>1,†</sup>

<sup>1</sup>*Terahertz Technology Innovation Research Institute, Terahertz Spectrum and Imaging Technology Cooperative Innovation Center, Shanghai Key Lab of Modern Optical System, University of Shanghai for Science and Technology, 516 Jungong Road, Shanghai 200093, China*

<sup>2</sup>*Key Laboratory of Terahertz Solid-State Technology, Shanghai Institute of Microsystem and Information Technology, Chinese Academy of Sciences, 865 Changning Road, Shanghai 200050, China*

<sup>3</sup>*Center of Materials Science and Optoelectronics Engineering, University of Chinese Academy of Sciences, Beijing 100049, China*

 (Received 22 April 2019; revised manuscript received 19 June 2019; published 19 August 2019)

Bias-polarity-dependent photocurrent spectra of a terahertz quantum-well photodetector with an asymmetric stepped-quantum-well absorption layer are explored both in theoretical and experimental aspects. The parameters of the stepped quantum well are designed to realize broadband detection that the photoresponse, corresponding to the electron transitions of ground subband ( $E_0$ ) to the first ( $E_1$ ) and second ( $E_2$ ) subbands, covers a broadband frequency range of 4.0–7.0 THz. Due to the asymmetric shape of the modulus squared wave functions of the  $E_2$  subband, the escape probability of the photoexcited electrons in subband  $E_2$  to continuum states is strongly bias-polarity dependent, which is responsible for the different shapes of photocurrent spectra with positive and negative bias voltages applied across the terahertz quantum-well photodetector. Our results show that not only the band structures, but also the wave functions play key roles in the analysis of the photoresponse of terahertz quantum-well photodetectors.

DOI: [10.1103/PhysRevApplied.12.024035](https://doi.org/10.1103/PhysRevApplied.12.024035)

### I. INTRODUCTION

In recent years, terahertz (THz) quantum-well photodetectors (QWP) based on intersubband transitions (ISBTs) have attracted more and more attention [1–3]. THz QWPs are important photon-type detectors operating in the THz spectral region, which have many unique advantages such as fast response [4], designable peak response frequency, easy integration, and high sensitivity over thermal-type detectors. Intensive investigations on the optimization of structural parameters, the design of light couplers with high efficiency [5–7], and the understanding of carrier transport properties for THz QWPs have been performed, and much progress has been achieved, which greatly improves the performance of THz QWPs [8].

In a conventional THz QWP, an  $n$ -doped multiquantum-well (MQW) absorption layer is sandwiched between two  $n$ -doped contact layers. There is an electron-occupied ground subband ( $E_0$ ) and an unoccupied (quasi) bound subband ( $E_1$ ) near the barrier edge. In the presence of a THz electric field with components perpendicular to the quantum-well (QW) plane, when THz photons with an

energy of about  $E_1 - E_0$  impinge on the THz QWP, ISBTs occur. The photon-excited electrons in subband  $E_1$  have a high probability to further transit into the continuum states above the barrier, and they drift across the device under an external bias voltage to form the photocurrent. At present, most of the investigations on improving the performance of a THz QWP focus on the optimization of QW width, barrier width, height, and carrier-doping concentration in the QWs for a given peak response frequency. Because of the inherent characteristics of ISBTs, a THz QWP based on one bound-bound ISBT is a narrowband detector (FWHM: approximately 1.5 THz). Bound-continuum transitions are beneficial to enhance the response bandwidth. However, the sensitivity of THz QWPs based on bound-continuum transitions deteriorates due to the decrease of the values of transition matrix elements. More than one unpopulated subband in a QW is helpful for increasing the response bandwidth. But for a symmetric QW, the ISBT selection rule prohibits the transitions between subbands  $E_0$  and  $E_{2n}$  with  $n$  as an integer. Even though the external bias voltage relaxes the ISBT selection rule to some extent, the transition strengths between subbands  $E_0$  and  $E_{2n}$  remain small.

Asymmetric QWs are a possible option for increasing the transition intensities of  $E_0 - E_{2n}$ . As the simplest

\*xgguo\_sh@qq.com

†ymzhu@usst.edu.cn

asymmetric quantum well, stepped QWs (SQWs) have been used to realize multicolor and bias-tunable QWPs. Fraenkal *et al.* studied the effect of an asymmetric SQW structure on detector performance [9–11]. Great efforts have been made to improve the responsivity and detectivity of asymmetric quantum-well infrared photodetectors, and to explore the inconsistency of photocurrent spectra under positive and negative bias voltages in the infrared spectral region, where it was believed that positive bias electrons have fewer reflections, shorter dwell time, and higher escape efficiency than negative bias electrons. In the THz spectral region, Wu *et al.* studied intersubband transitions in GaN/(Al,Ga)*N* SQWs [12]. Wang *et al.* designed, fabricated, and characterized a broadband bias-tunable THz QWP with an asymmetric-SQW absorption layer [13]. In a THz QWP with similar device structural parameters as reported in Ref. [13], we first find that the photoresponse of the THz QWP is strongly bias-polarity dependent, and we attribute such a behavior to the asymmetric wave function of the third subband in the SQW that introduces the bias-polarity-dependent recapture and escape probabilities of photoexcited electrons. Our investigations provide an alternative way to improve the performance of THz QWPs and to design alternative terahertz quantum devices, for example, photon-mediated diodes in the THz regime.

In this work, we design and fabricate a GaAs/(Al,Ga)As THz QWP with an absorption layer composed of multi-SQWs. The bias-polarity-dependent behavior of the photocurrent spectrum is systemically investigated. Because of good matching of the lattice constants of GaAs and (Al,Ga)As with a large variation in the Al mole fraction, SQWs with high-quality heterojunction interfaces can be grown by the molecular beam epitaxy (MBE) technique. Such high-quality GaAs/(Al,Ga)As SQWs not only ensure high sensitivity of the THz QWP, but also make them an ideal model system to study the THz-field-assisted electron vertical transport properties across the device [14]. There are 22 identical SQWs in the absorption layer of the designed THz QWP. In each SQW, three bound subbands ( $E_0$ ,  $E_1$ , and  $E_2$ ) exist with the ground subband ( $E_0$ ) populated by localized electrons and the other two ( $E_1$  and  $E_2$ ) unpopulated. At low bias voltages, due to the bias-dependent escape properties of THz-excited electrons in  $E_1$  and  $E_2$  subbands, the photocurrent spectra show bias-tunable characteristics, while at high bias voltages, the photoresponse covers a broadband of 4.0–7.0 THz because most of the electrons in subbands  $E_1$  and  $E_2$  are swept to the continuum states. It is interesting to note that the photocurrent spectra are remarkably bias-polarity dependent, especially in the frequency range of 5.0–6.5 THz corresponding to the  $E_0 - E_2$  ISBT. Dark current-voltage ( $I$ - $V$ ) measurements show that there is no measurable built-in electric field. Our investigations show that the structural asymmetry (SQWs) plays different roles in the transport

behaviors of drift electrons above the barrier (symmetric dark  $I$ - $V$  curve) and the photoexcited electrons (bias-polarity-dependent photocurrent spectra). The calculation of band structures shows that the asymmetric wave function of subband  $E_2$  introduces the bias-polarity-dependent escape rates of photoexcited electrons in subband  $E_2$ , which is responsible for the bias-polarity-dependent photocurrent spectra.

## II. DEVICE DESIGN, FABRICATION, AND DARK CURRENT

The material structure of the designed THz QWP is shown in Fig. 1(a). One 250-nm GaAs buffer layer is grown on a GaAs substrate, followed by one 800-nm *n*-doped GaAs bottom contact layer with a Si doping concentration of  $1 \times 10^{17} \text{ cm}^{-3}$ . The following is the absorption layer composed of 22 periods of SQWs. Each SQW consists of one 19-nm GaAs well with a Si doping concentration of  $6 \times 10^{16} \text{ cm}^{-3}$  in the central 10-nm region of the well, one 19-nm  $\text{Al}_{0.022}\text{Ga}_{0.978}\text{As}$  layer, and one 100-nm  $\text{Al}_{0.041}\text{Ga}_{0.959}\text{As}$  barrier layer. Finally, one 400-nm GaAs top contact layer with the same doping concentration as the bottom contact layer is grown. Due to the selection rule of ISBT, when the incident THz beam is perpendicular to the device surface, the electric field perpendicular to the growth direction of the QWs cannot induce the ISBT of confined electrons in the SQWs. Therefore, a one-dimensional metallic grating coupler is fabricated on the top contact layer of the device, which changes the propagation direction of the vertical incident THz beam and generates a polarization component that is parallel to the growth direction of the SQWs. The period of the grating coupler is  $18 \mu\text{m}$  and the duty cycle is 50%. The designed Al mole fractions in the shallower QW layers and the barrier layers are 2.00% and 2.76%, respectively, which promises that the subband  $E_2$  is resonant with the barrier. Because it is difficult to precisely control the low Al concentrations during the MBE growth, the Al mole fractions in the shallower quantum-well and barrier layers are verified by fitting the experimental photoluminescence data of the epitaxy wafer. A deviation of a realistic Al mole fraction (4.1%) in the barrier layers from the designed value (2.76%) is found. The band structures are numerically calculated with the Al mole fractions derived from the photoluminescence data. The deviation of the Al mole fraction in barrier layers does not affect the main results and conclusions of this work. The other parameters, such as the width of SQWs, the Si-doping concentrations in the SQWs, and the contact layers, can be accurately controlled during the MBE growth.

The band structure of the SQW is numerically calculated by self-consistently solving the Schrödinger equation and the Poisson equation. The many body effects [15] are considered within the local-density approximation. Figure 1(b)

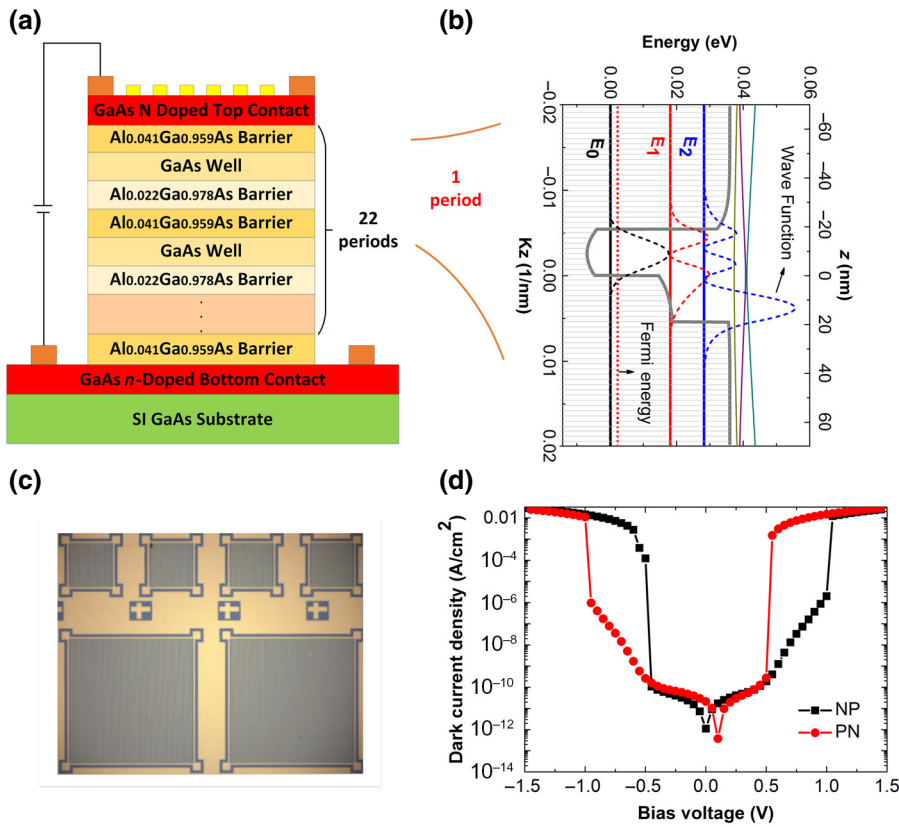


FIG. 1. (a) Structural schematic of the THz QWP. (b) Band structure and modulus squared wave functions for subbands  $E_0$ ,  $E_1$ , and  $E_2$  of the SQW under zero bias voltage. (c) Microphotograph of the device. (d) Dark  $I$ - $V$  characteristics of the THz QWP immersed in liquid helium. (The red circular line (PN) represents the voltage sweeping from positive to negative values; the black square line (NP) represents the voltage sweeping from negative to positive values.)

shows the potential distribution, subbands, Fermi energy, and the modulus squared wave functions for subbands  $E_0$ ,  $E_1$ , and  $E_2$  of the SQW under zero bias voltage. Due to the deviation of the Al mole fraction in the barrier layers, the subband  $E_2$  is obviously lower than the top of the barrier layer. The peak photoresponse frequencies of the designed device are around 4.4 THz (ISBT of  $E_0 - E_1$ ) and 6.8 THz (ISBT of  $E_0 - E_2$ ).

The devices are fabricated using the standard GaAs processing techniques. The epitaxial wafer is first cleaned, and the photoresist mask pattern of the mesa is formed by steps of coating, photolithography, development, and wet etching. For the GaAs/(Al, Ga)As wet-etching process, the  $\text{H}_3\text{PO}_4/\text{H}_2\text{O}_2$  etching solution is used, and the ratio is  $\text{H}_3\text{PO}_4 : \text{H}_2\text{O}_2 : \text{H}_2\text{O} = 1:1:25$  (where the water is 500 mL). There will be some difference in the rate of wet etching at different environmental temperatures, so it is necessary to carry out multiple etching steps in order to control the etching depth in the process of wet etching. For the THz QWP, we select Ge/Au/Ni/Au as the top and bottom electrodes. First, the electrode pattern is formed by photolithography, then Ge, Au, Ni, and Au are sequentially deposited by electron beam evaporation, and finally, the electrodes are formed by a lift-off process. The Ti/Au metallic grating is fabricated with the same process. The fabricated device is divided into mesas of  $1000 \times 1000 \mu\text{m}^2$ , and is packaged on low-temperature sample holders through wire bonding. Figure 1(c) presents

the mesa micrograph of THz QWPs integrated with one-dimensional metallic strip gratings.

A dark  $I$ - $V$  curve is a key quantity in determining the performance of a THz QWP. Hot-electron emission, direct tunneling, and scattering assistant processes are the three main mechanisms of dark current in QWPs. While in the THz frequency range, the main dark current generation mechanisms are hot-electron emission and scattering assistant processes, especially under the conditions of wide barrier, low bias, and low temperature. Figure 1(d) shows the dark  $I$ - $V$  curves of the THz QWP measured in voltage-sweeping mode at a temperature of 4.2 K. Under different bias sweeping directions (PN represents sweeping from positive to negative, and NP represents the inverse sweeping direction), there are two obvious jump regions in the dark  $I$ - $V$  curves. The jump regions are related to the negative differential resistance (NDR) effect. This effect may be due to the interaction between conducting electrons and bound electrons, which results in the heating of bound electrons or subband collision ionization [16,17]. The discrepancy between the minimum current and zero bias voltage points in the dark  $I$ - $V$  curves originates in the non-Ohmic metal-semiconductor contacts and the deviation of Si-doping position from the central regions of the deeper left QWs during the material growth. The dark  $I$ - $V$  curves measured in the NP and PN sweeping directions can be divided into two symmetric groups. One group includes the sections of N0 (negative value to zero) and P0 (positive

value to zero), and the other group includes the sections of 0N (zero to negative value) and 0P (zero to positive value). The two symmetric groups of dark  $I$ - $V$  curves indicate that there is no notable built-in electric field in the device.

### III. BIAS-POLARITY-DEPENDENT PHOTOCURRENT SPECTRA

The experimental setup for measuring the photocurrent spectra of the THz QWP is shown in Fig. 2(a). The photocurrent spectra of the device are measured as follows. The THz radiation emitted by a built-in infrared source (Globar) of a FTIR (Bruker, VERTEX 80V) is passed through a pinhole and is collimated by an off-axis parabolic mirror. The collimated THz beam enters into a Michelson interferometer with a 6- $\mu\text{m}$ -Mylar beam splitter. The modulated interference THz beam is focused by an off-axis parabolic mirror on the THz QWP mounted in an optical cryostat (Oxford, CF-V). A low-noise current preamplifier (Stanford, SR570) is used to apply a constant bias voltage to the device. The photocurrent signal induced by the interference THz beam is amplified by the current amplifier. The photocurrent interferograms are recorded and Fourier transformed by a computer, and finally the photocurrent spectra are obtained [Fig. 2(b)]. The measurements of photocurrent spectra are carried out in a vacuum chamber to avoid the influence of water vapor absorption at the temperature of 4.2 K.

The photocurrent spectra at different negative and positive bias voltages are presented in Fig. 2(b). The bottom contact in Fig. 1(a) is grounded for both negative and positive bias voltages. For each absolute value of bias voltage, the pair of photocurrent spectra at positive and negative biases are normalized to the peak value of photocurrent under the negative bias. The bias voltage is swept in the directions of 0P and 0N as defined in Fig. 1(d). The peak response frequencies of the THz QWP are about 4.5 THz (ISBT of  $E_0 - E_1$ ) and 6.5 THz (ISBT of  $E_0 - E_2$ ), which are slightly different from the designed values of 4.4 THz (ISBT of  $E_0 - E_1$ ) and 6.8 THz (ISBT of  $E_0 - E_2$ ). Such discrepancies of peak response frequencies should be introduced by the approximation for dealing with the many body effects or from the deviation of the Al mole fraction during MBE growth of the device structure. In the spectral region of 4.4–6.8 THz, the photoresponse can be attributed to the broadening of subbands  $E_1$  and  $E_2$ , which corresponds to the fluctuation of QW parameters (well width and Al mole fraction) and impurity and interface scattering processes. For both polarities of bias voltage, the photocurrent spectra show bias-tunable characteristics. At low bias voltages ( $\pm 0.2$  and  $\pm 0.4$  V), the photoresponse is in the frequency range of 5.0–7.5 THz, which corresponds to the ISBT of  $E_0 - E_2$ . Because the escape probability of photoexcited electrons in subband  $E_1$  is very small at low bias

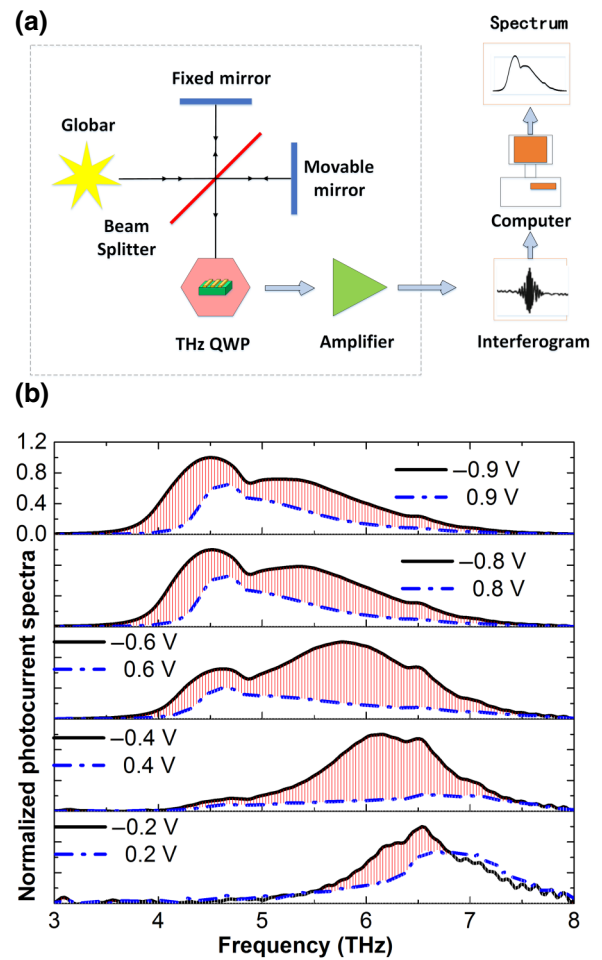


FIG. 2. (a) Schematic of experimental setup for measuring the photocurrent spectra of THz QWP. (b) Photocurrent spectra at different positive and negative bias voltages. For both polarities of bias voltage, the bottom contact of the device is grounded. The solid black lines represent the spectra at negative bias voltages, and the dash-dot blue lines represent the spectra at positive bias voltages.

voltages, and most of them will relax to the ground subband  $E_0$ , the photoresponse in the lower frequency range of 4.0–5.0 THz can be neglected. However, at higher bias voltages ( $\pm 0.6$ ,  $\pm 0.8$ , and  $\pm 0.9$  V), field-assisted thermal emission (through acoustic phonon emission electron-phonon scattering processes) and tunneling result in the increase of the escape rate of photoexcited electrons in subband  $E_1$  and then the photoresponse in the range of 4.0–5.0 THz.

At the same time, we can obviously observe that the shapes of the photocurrent spectra of the device are very different at positive and negative bias voltages with the same absolute value. The differences are most pronounced at the bias voltages of 0.4 and 0.6 V, and the maximum ratio of photocurrent under  $-0.4$  and  $0.4$  V is about 7.0 at 5.9 THz. Such a behavior of bias-polarity-dependent

photoresponse can be considered as a THz-assisted current rectification effect. However, at higher bias voltages, the shape difference between the two photocurrent spectra at the same absolute value of bias voltages but with opposite polarities becomes smaller. In general, the photocurrent spectrum of the device is determined by ISBT absorption spectrum, the escape probability of the photoexcited electrons, and the photoconductive gain [2]. Intuitively, without considering the linear Stark effect [18], the polarity of the bias should not obviously affect the photocurrent spectrum, but from the experimental results, we do observe that the shape of the spectrum depends on the polarity of the bias voltage, which is a very special and interesting phenomenon. Dark current measurements show that there are no built-in electric fields in the device. Therefore, the bias-polarity-dependent photocurrent spectra do not originate in the drift of photoexcited electrons above the energy barrier. Instead, the bias-polarity-dependent band structure and electron scattering processes between subbands  $E_1$  and  $E_2$  and between subband  $E_2$  and the quasi-continuum states should be responsible for the bias-polarity-dependent behavior of photocurrent spectra.

The band structures and wave functions of the THz QWP at bias voltages of  $\pm 0.6$  V are numerically calculated [15]. A periodic boundary condition is adopted. Because the global symmetry is broken by the bias voltage, an artificial triangular well is introduced in the computational domain when the periodic boundary condition is applied. In order to reduce the undesirable effects of the periodic boundary condition on the localized wave functions corresponding to subbands  $E_0$ ,  $E_1$ , and  $E_2$ , three SQWs are considered in our numerical calculations. Figure 3 presents the subbands and the corresponding modulus squared wave functions of the asymmetric SQWs at bias voltages of  $\pm 0.6$  V. Because Si atoms are doped in the central 10-nm region of the left deeper wells of the SQWs, electron distributions in the wells are different between positive and negative bias voltages, which also leads to the different distributions of Hartree potentials for the two bias polarities. At a bias voltage of 0.6 V, the subband  $E_2$  is lifted up to the edge of barrier and the energy differences between  $E_0 - E_1$  and  $E_1 - E_2$  are larger than the corresponding ones at a bias voltage of  $-0.6$  V, which is in good agreement with the experimental results where the peak response frequencies at negative bias voltage are lower than those at positive bias voltage with the same absolute value. The escape probability  $p_e(E)$  of photoexcited electrons in subband  $E_2$  can be expressed as [19]

$$p_e(E) = \frac{\Gamma_e(E)}{\Gamma_e(E) + \Gamma_r(E)}, \quad (1)$$

where  $E$  is the energy of the photoexcited electrons in subband  $E_2$ ,  $\Gamma_e$  and  $\Gamma_r$  are the scattering rates between the subband  $E_2$  and the quasi-continuum states and the

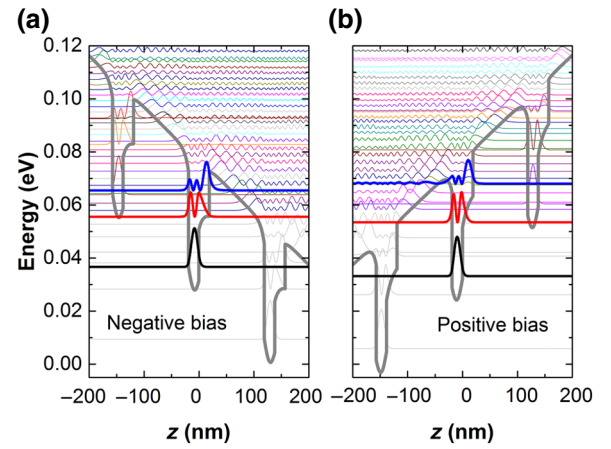


FIG. 3. The modulus squared wave functions of the asymmetric SQWs under negative (a) and positive (b) bias voltages.

capture rate of photoexcited electrons in subband  $E_2$ , respectively. On the basis of band structure calculations, the bias-polarity-dependent photocurrent spectra shown in Fig. 2(b) can be qualitatively explained as follows. First, for both bias polarities, the modulus squared wave functions for subband  $E_2$  show remarkable asymmetry, and the largest peak is located in the shallower QW, which indicates that the photoexcited electrons in subband  $E_2$  tend to populate on the right side of the SQW. For positive biases, the photoexcited electrons have a larger dwell time when they transport across the SQW, which will lead to a larger value of  $\Gamma_r$  and then a smaller value of  $p_e$ . Further, there are larger overlap integrals of wave functions between subband  $E_2$  and continuum states, which results in a larger scattering rate  $\Gamma_e$  and escape probability  $p_e$  of photoexcited electrons in subband  $E_2$  under negative bias voltages [20]. On the contrary, for positive bias voltages, the photoexcited electrons in subband  $E_2$  will relax to the ground subband  $E_0$  with a greater probability. At the same time, because subband  $E_2$  is lower than the barrier edge, the escape probability and then the photocurrent are more sensitive to the value of bias voltage, which is in accordance with the experimental data shown in Fig. 2(b). Second, it is expected that there is a portion of photoresponse in the 5.0–6.5 THz range originating in the intersubband ( $E_1 - E_2$ ) scattering of photoexcited hot electrons in subband  $E_1$ . As shown in Fig. 3, at a bias voltage of  $-0.6$  V, because of the smaller energy difference between  $E_1$  and  $E_2$ , the intersubband  $E_1 - E_2$  scattering is more effective, which further enhances the photoresponse in the frequency range of 5.0–6.5 THz.

Bias-dependent responsivity [9,10] and electrical tunable peak response frequency [21] in stepped-quantum-well infrared photodetectors have been reported. In Ref. [9], the bias-polarity-dependent saturation of responsivity was observed. But the shape of the photocurrent spectrum

does not show obvious bias-polarity dependence, which is very different from our experimental results. The bias-dependent responsivity was attributed to the bias-induced difference of transmission and/or reflection (dwell time in the QW layer) at the GaAs/(Al, Ga)As interfaces. However, in this work, the symmetric dark  $I$ - $V$  curve indicates that the transmission (reflection) probability does not show remarkable bias-polarity dependence. The reason is the large difference of Al mole fractions (present work: 0.041/0.022, Ref. [9]: 0.35/0.20). In Ref. [21], a bias-tunable peak response frequency was observed, and this behavior was attributed to the linear Stark shift of intersubband transitions [22]. However, no bias-polarity-dependent photocurrent spectra were observed. The reason is that there are only two localized subbands [21]. Our analysis shows that the third localized subband plays a key role in the bias-polarity-dependent photocurrent spectra.

Except for the zero-built-in field, there are two other reasons responsible for the symmetric dark  $I$ - $V$  curve. First, in the dark condition, because of the low energy difference between the ground subband and the continuum states and low bias voltage ( $<4.0$  kV/cm), the capture of drift electrons in the QW layers via longitudinal optical phonon emission is not so efficient. In steady state, the capture rate of drift electrons equals the thermal emission rate of confined electrons, which indicates that at low temperature, the capture and thermal emission rates are all low, and the asymmetric wave function of subband  $E_2$  plays a minor role in the transport behavior of drift electrons. Second, there are different channels for the capture of drift electrons and thermal emission of confined electrons, which further weaken the effect of the asymmetric wave function of subband  $E_2$  on the transport behavior of drift electrons. When THz waves impinge on the device, the confined electrons have extra probabilities to escape from the SQWs via intersubband transitions. The depletion of confined electrons in the QWs will lead to the enhancement of local electric fields, which will increase the capture rate of the hotter drift electrons (obtaining more energy from the higher local electric field) via LO phonon emission. Because of these microscopic processes, the bias-polarity-dependent photocurrent spectra are introduced by the asymmetric wave function of subband  $E_2$ .

#### IV. CONCLUSION

In conclusion, in a bias-tunable and broadband THz QWP with an asymmetric-SQW absorption layer, the bias-polarity-dependent photocurrent spectra are found and systematically analyzed both in experimental and theoretical aspects. The symmetric dark  $I$ - $V$  characteristics show that there is no built-in electric field across the device and the dwell time of drift electrons in the SQW layers is not dependent on the bias polarity. Therefore, the bias-polarity-dependent spectra do not originate in the drift of

photoexcited electrons above the energy barrier. By calculating the modulus squared wave functions at the bias voltages of  $\pm 0.6$  V, it is found that the shape of the wave functions of the  $E_2$  subband is strongly asymmetric under positive and negative bias voltages, which results in the polarity dependent probabilities of escape and recapture of the photoexcited electrons in subband  $E_2$  and then the bias-polarity-dependent photocurrent spectrum. Our results show that not only the band structures, but also the asymmetric distribution of wave functions play key roles in the design of broadband THz stepped-quantum-well photodetectors with high performance.

#### ACKNOWLEDGMENTS

This work was supported in part by the National Natural Science Foundation of China (Grants No. 61731020, No. 61722111, and No. 61775229), the National Key Research and Development Program of China (Grant No. 2017YFA0701005), the 111 Project (Grant No. D18014), the International Joint Lab Program supported by Science and Technology Commission Shanghai Municipality (Grant No. 7590750300), and the Young Yangtze Rive Scholar (Grant No. Q2016212).

- 
- [1] H. C. Liu, C. Y. Song, A. J. SpringThorpe, and J. C. Cao, Terahertz quantum-well photodetector, *Appl. Phys. Lett.* **84**, 4068 (2004).
  - [2] H. Schneider and H. C. Liu, *Quantum Well Infrared Photodetectors: Physics and Applications* (Springer, New York, 2007).
  - [3] X. G. Guo, J. C. Cao, R. Zhang, Z. Y. Tan, and H. C. Liu, Recent progress in terahertz quantum-well photodetectors, *IEEE J. Sel. Top. Quant. Electron.* **19**, 8500508 (2013).
  - [4] H. Li, W. J. Wan, Z. Y. Tan, Z. L. Fu, H. X. Wang, T. Zhou, Z. P. Li, C. Wang, X. G. Guo, and J. C. Cao, 6.2 GHz modulated terahertz light detection using fast terahertz quantum well photodetectors, *Sci. Rep.* **7**, 3452 (2017).
  - [5] J. Y. Andersson and L. Lundqvist, Grating-coupled quantum-well infrared detectors: Theory and performance, *J. Appl. Phys.* **71**, 3600 (1992).
  - [6] R. Zhang, X. G. Guo, C. Y. Song, M. Buchanan, Z. R. Wasilewski, J. C. Cao, and H. C. Liu, Metal grating coupled terahertz quantum well photodetectors, *IEEE Electron Device Lett.* **32**, 659 (2011).
  - [7] R. Zhang, X. G. Guo, J. C. Cao, and H. C. Liu, Near field and cavity effects on coupling efficiency of one-dimensional metal grating for terahertz quantum well photodetectors, *J. Appl. Phys.* **109**, 073110 (2011).
  - [8] S. Zhang, T. M. Wang, M. R. Hao, Y. Yang, Y. H. Zhang, W. Z. Shen, and H. C. Liu, Terahertz quantum-well photodetectors: Design, performance, and improvements, *J. Appl. Phys.* **114**, 194507 (2013).
  - [9] A. Fraenkel, A. Brandel, G. Bahir, E. Finkman, G. Livescu, and M. T. Asom, Bias dependence of responsivity and

- transport in asymmetric quantum well infrared detectors, *Appl. Phys. Lett.* **61**, 1341 (1992).
- [10] A. Fraenkel, A. Brandel, G. Bahir, and E. Finkman, in *Infrared Detectors: State of the Art, SPIE 1735*, p. 217 (1992).
- [11] A. Brandel, A. Fraenkel, E. Finkman, G. Bahir, G. Livescu, and M. T. Asom, Responsivity and thermionic current in asymmetric quantum well infrared detectors, *Semicond. Sci. Technol.* **8**, S412 (1993).
- [12] F. Wu, W. Tian, W. Y. Yan, J. Zhang, S. C. Sun, J. N. Dai, Y. Y. Fang, Z. H. Wu, and C. Q. Chen, Terahertz intersubband transition in GaN/AlGaIn step quantum well, *J. Appl. Phys.* **113**, 154505 (2013).
- [13] H. X. Wang, Z. L. Fu, D. X. Shao, Z. Z. Zhang, C. Wang, Z. Y. Tan, X. G. Guo, and J. C. Cao, Broadband bias-tunable terahertz photodetector using asymmetric GaAs/AlGaAs step multi-quantum well, *Appl. Phys. Lett.* **113**, 171107 (2018).
- [14] A. Fraenkel, E. Finkman, S. Maimon, and G. Bahir, Vertical drift mobility of excited carriers in multi quantum well structures, *J. Appl. Phys.* **75**, 3536 (1994).
- [15] X. G. Guo, Z. Y. Tan, J. C. Cao, and H. C. Liu, Many-body effects on terahertz quantum well detectors, *Appl. Phys. Lett.* **94**, 201101 (2009).
- [16] A. Delga, L. Doyennette, A. Buffaz, V. Berger, F. R. Jasnot, L. A. De Vaulchier, N. Péré-Laperne, and H. C. Liu, Space charge mediated negative differential resistance in terahertz quantum well detectors, *J. Appl. Phys.* **110**, 013714 (2011).
- [17] X. G. Guo, L. L. Gu, M. Dong, J. C. Cao, H. C. Liu, and F. M. Guo, Negative differential resistance induced by thermalization of two-dimensional electrons in terahertz quantum-well photodetectors, *J. Appl. Phys.* **113**, 203109 (2013).
- [18] M. Helm, The basic physics of intersubband transitions, in *Intersubband Transitions in Quantum Wells Physics and Device Applications I*, H. C. Liu and F. Capasso, eds (Academic, San Diego, CA, 2000).
- [19] B. F. Levine, A. Zussman, S. D. Gunapala, M. T. Asom, J. M. Kuo, and W. S. Hobson, Photoexcited escape probability, optical gain, and noise in quantum well infrared photodetectors, *J. Appl. Phys.* **72**, 4429 (1992).
- [20] C. Jacoboni and P. Lugli, *The Monte Carlo Method for Semiconductor Device Simulation* (Springer, Wien, 1989).
- [21] E. Martinet, F. Luc, E. Rosencher, Ph. Bois, and S. Delaitre, Electrical tunability of infrared detectors using compositionally asymmetric GaAs/AlGaAs multiquantum wells, *Appl. Phys. Lett.* **60**, 895 (1992).
- [22] Y. J. Mii, R. P. G. Karunasiri, K. L. Wang, M. Chen, and P. F. Yuh, Large Stark shifts of the local to global state intersubband transitions in step quantum wells, *Appl. Phys. Lett.* **56**, 1986 (1990).